PAPER

Promotional mechanism of enhanced denitration activity with Cu modification in a Ce/TiO₂–ZrO₂ catalyst for a low temperature NH₃-SCR system†

Wei Zhang, [ID] *[ab] Yunhao Tang,[ab] Wei Xiao,[ab] Min Ruan,[ab] Yanshan Yin,[ab] Quanbin Song,[ab] Kang Xie,[ab] Chuan Qin,[ab] Mengyao Dong,[ab] Yunhe Zhou[ab] and Jie Li*[ab]

This study aims to investigate the enhanced low temperature denitration activity and promotional mechanism of a cerium-based catalyst through copper modification. In this paper, copper and cerium oxides were supported on TiO_2–ZrO_2 by an impregnation method, their catalytic activity tests of selective catalytic reduction (SCR) of NO with NH_3 were carried out and their physicochemical properties were characterized. The $CuCe/TiO_2$–ZrO_2 catalyst shows obviously enhanced NH_3-SCR activity at low temperature (<300 °C), which is associated with the well dispersed active ingredients and the synergistic effect between copper and cerium species ($Cu^{2+} + Ce^{3+} \leftrightarrow Cu^+ + Ce^{4+}$), and the increased ratios of surface chemisorbed oxygen and Cu^+/Cu^{2+} lead to the enhanced low-temperature SCR activity. The denitration reaction mechanism over the $CuCe/TiO_2$–ZrO_2 catalyst was investigated by *in situ* DRIFTS and DFT studies. Results illustrate that the NH_3 is inclined to adsorb on the Cu acidic sites (Lewis acid sites), and the NH_2 and NH_2NO species are the key intermediates in the low-temperature NH_3-SCR process, which can explain the promotional effect of Cu modification on denitration activity of Ce/TiO_2–ZrO_2 at the molecular level. Finally, we have reasonably concluded a NH_3-SCR catalytic cycle involving the Eley–Rideal mechanism and Langmuir–Hinshelwood mechanism, and the former mechanism dominates in the NH_3-SCR reaction.

1. Introduction

Nitrogen oxides (NO_x) from automobile exhaust emissions and industrial processes can cause harmful effects on the ecological environment, such as photochemical smog, ozone depletion, acid rain, and the greenhouse effect.[1,2] The selective catalytic reduction of NO_x with NH_3 (NH_3-SCR) is the most efficient and widely used technology for the control of NO_x emission.[3,4] Traditional commercial vanadium–titanium catalysts have been used in various industrial fields due to their stability and high efficiency, but industrial application is still restrained by their inevitable drawbacks, including high operation temperature window, poisoning and deactivation of catalyst by deposited alkaline metal, and vanadium poisoning.[5–7] Therefore, it is necessary to develop NH_3-SCR catalysts with excellent denitration activity in low temperature ranges.

Due to its preferable oxygen storage and redox properties, cerium-based catalyst has been extensively investigated to eliminate NO_x during the past several years.[8] However, the NH_3-SCR activity of pure ceria is still very low, it is necessary to dope other transitional metals to improve the denitration performance of CeO_2. Copper containing materials have been commonly employed as catalysts due to the good low-temperature activity in NH_3-SCR process. Among them catalysts modified with copper, such as Cu-ZSM-5,[9] Cu-MCM-41,[10] Cu/SAPO-34,[11] and Cu/TiO₂ (ref. 12) have presented a high catalytic activity in the low temperature range. Moreover, it is reported that the synergistic interaction between Cu with Ce species can contribute to the enhancement of low temperature catalytic activity.[13] Understanding the reaction mechanism over the catalyst is one of the core interests for the development of the NH_3-SCR catalyst with high catalytic activity. The generally accepted NH_3-SCR reaction mechanism includes two mechanisms in low temperature section, Eley–Rideal mechanism (adsorbed NH_3 reacts with gaseous NO and then decomposes to N_2 and H_2O) and Langmuir–Hinshelwood mechanism (adsorbed NO reacts with adsorbed NH_3 on the adjacent sites and then decomposes to N_2 and H_2O).[14,15] Previously, it has been shown that a mixed Eley–Rideal mechanism and Langmuir–Hinshelwood mechanism for NH_3-SCR reaction over Cu/SSZ-39 catalyst

[a] College of Energy and Power Engineering, Changsha University of Science & Technology, Changsha, 410114, China. E-mail: weizhang@csust.edu.cn

[b] Key Laboratory of Renewable Energy Electric-Technology of Hunan Province, Changsha, 410114, China

at low temperature.[16] Moreover, Lewis acid sites on the Cu–Ce-USY catalyst surface play a crucial role in its excellent low temperature SCR performance.[17] Although there are many studies on reaction mechanism of copper and copper–cerium catalysts, details on reaction path and mechanism still need to be further investigated.

In addition to the experimental methods, the quantum chemical theoretical calculation methods of molecular simulation, especially the density functional theory (DFT), has been widely used to study the reaction mechanism in the field of catalyst denitration.[18] On the one hand, the theoretical calculations can solve several problems difficultly dealt with the experimental study, such as active intermediates and molecular reaction details. On the other hand, the mutual verification with the experimental results improves the credibility of the experiment. As the first step and important part in the SCR reaction, the NH_3 and NO adsorption are related to the active acid sites and can lead to the generation of highly active intermediaries, which can be well discussed with DFT calculations.

In this paper, we explored the promotional mechanism of enhanced denitration activity on the cerium-based catalyst with copper modification for low temperature NH_3-SCR reaction. Textural, morphological and redox properties of the catalysts were researched with a few physicochemical characterized measurements, such as XRD, SEM, and XPS techniques. The active adsorbed species and intermediates were detected with *in situ* diffuse reflectance infrared Fourier transform spectroscopy (*in situ* DRIFTS), and the adsorptions of NH_3 and NO molecules were calculated with DFT method. The NH_3-SCR reaction mechanism over CuCe/TiO$_2$–ZrO$_2$ catalyst was systematically investigated by the *in situ* DRIFTS measurements combined with DFT calculations, and the catalytic cycle was deduced. Elucidating the NH_3-SCR reaction mechanism over CuCe/TiO$_2$–ZrO$_2$ catalyst in the molecular level could provide theoretical guidance for the design and development of modification on denitration catalysts.

2. Experimental and computational details

2.1 Catalyst preparation

The CuCe/TiO$_2$–ZrO$_2$ catalyst was prepared by impregnation method, and the amount of copper and cerium loading on the TiO$_2$–ZrO$_2$ support were 20 wt% and 10 wt%, respectively. The TiO$_2$–ZrO$_2$ (molar ratio of 1 : 1) support was synthesized by sol–gel method. Firstly, a certain quantity of $Ti(OC_4H_9)_4$ and $ZrOCl_2\cdot 8H_2O$ (Guoyao Group Chemical Reagent Co., Ltd.) were dissolved in ethanol absolute, followed by dropwise addition of pre-prepared solution (the deionized water : acetic acid : ethanol absolute = 2 : 2 : 1 volume ratio). As addition of pre-prepared solution progressed to a certain extent, the precursor solution gradually became transparent and the pH of the solution increased to around 2. Afterwards, the mixed solution was stirred magnetically at room temperature until transparent sol was formed. Next, the mixture heated in a thermostatic water bath at 50 °C for 1 h and aged at room temperature for 12 h till

the hydrosol became transparent gel. Finally, the gel was incubated at 80 °C for 5 h and kept at 120 °C overnight in an oven. The obtained product was ground and calcined at 500 °C for 3 h in the muffle furnace. Certain amount of $Ce(NO_3)_3\cdot 6H_2O$ (Tianjin Guangfu Fine Chemical Research Institute) and TiO$_2$–ZrO$_2$ were dissolved in deionized water, then the solution with magnetic stirring at 80 °C for 1 h. The obtained product was aged at room temperature for 12 h. Then, the mixture dried at 105 °C overnight in the oven and calcined at 450 °C for 4 h in a muffle furnace to obtain the Ce/TiO$_2$–ZrO$_2$ catalyst. The Cu/TiO$_2$–ZrO$_2$ catalyst was prepared with $Cu(NO_3)_2\cdot 3H_2O$ (Tianjin Fuchen Chemical Reagents Company) and TiO$_2$–ZrO$_2$ as precursors followed the same method. The Ce/TiO$_2$–ZrO$_2$ sample and corresponding amount of $Cu(NO_3)_2\cdot 3H_2O$ were dissolved in deionized water, then through magnetic stirring, evaporation, and calcination as with the above preparation method, and the catalyst prepared was denoted as CuCe/TiO$_2$–ZrO$_2$.

2.2 Catalyst activity test

The catalyst activity tests were carried out in a bench-scale experimental system at the temperature range of 150–400 °C. During each test, 0.2 g catalyst was put in the quartz tube of tubular furnace filled with the simulated flue gas. The reactant gas mixture contained 500 ppm NO, 500 ppm NH_3, 5% O_2 and N_2 balanced, and the total flow rate of the feeding gas was 500 mL min^{-1}, corresponding to a gas hourly space velocity (GHSV) of 60 000 h^{-1}. During each catalytic test, the temperature reached around the preset value, then reaction continued for 10 min until the readings of temperature and NO concentration were stable. Afterwards, the temperature and NO concentration were recorded every 30 s in 5 min, the average value was calculated and used to obtain the NO conversion. NO concentrations in the inlet and outlet gas were collected with a professional flue gas analyzer (Madur Photon & PGD-100, Austria). The denitration activity was determined by NO conversion, which was calculated by the following equation:

$$NO \ conversion = \frac{NO(in) - NO(out)}{NO(in)}$$

where NO (in) represented the NO concentration in the feed gas and NO (out) expressed the NO concentration in the effluent stream.

2.3 Catalyst characterization

The X-ray diffraction (XRD) patterns of the different catalysts were collected with a D8 Advanced diffractometer (Bruker, Germany) with Cu Kα radiation in the 2θ range from 10° to 80°. The working voltage was 40 kV, and the working current was 30 mA.

The Scanning electron microscopy (SEM) images of the samples were taken with a Quanta 250 FEG scanning electron microscope (FEI, USA) at an accelerating voltage of 30 kV.

The X-ray photoelectron spectroscopy (XPS) measurements were recorded on an Axis Ultra DLD spectrometer (Kratos, UK), Al Kα radiation was used as the excitation source. The binding

energies were corrected by C1s peak at 284.6 eV to compensate the charging effect.

In situ DRIFTS experiments were performed on a Nicolet iS 50 FTIR spectrometer (Thermo Fisher, USA) equipped with an MCT/A detector. The catalyst was pretreated in the cell at 400 °C for 1 hour to remove adsorbed impurities, and then cooled down to 200 °C in N_2 gas flow. The background spectrum was recorded in a flow of pure N_2 atmosphere and subtracted automatically from the catalyst sample at 200 °C.

2.4 DFT calculations

The structural optimization, intermediates, transition states search, and calculated energy were analyzed in the DMol3 module in Materials Studio 2019. The generalized gradient approximation (GGA) with the Perdew–Burke–Ernzerhof (PBE) functional was used to describe the electron exchange–correlation potential.[19] The interaction between the valence and the core electrons was described by the projector augmented wave (PAW).[20] Brillouin zone was sampled by employing the $2 \times 2 \times 1$ Monkhorst–Pack k-point grid and the plane wave cutoff energy was 400 eV. The maximum force of geometry optimization to 0.05 eV Å^{-1}. The convergence tolerance values of total energy, maximum atomic forces and maximum displacement were 1×10^{-5} Hartree, 4×10^{-3} Hartree Å^{-1} and 5×10^{-3} Å, respectively.[21]

CeO_2 (1 1 1) has been previously reported to be the most stable among low index CeO_2 facets,[22,23] which is also in harmony with the experimental result in this paper. Therefore, the low-doped copper–ceria surface model was obtained from a CeO_2 (1 1 1) slab, with a p (3 × 3) expansion of the surface unit cell, by substituting one surface Ce atom by one Cu atom. The optimized lattice parameters of the three-layer model were $a = b = 11.64$ Å, $c = 26.71$ Å, containing a vacuum layer of 20 Å set in the vertical direction to minimize the interaction between neighboring slab surfaces.

The adsorption energy was evaluated to characterize the adsorption properties of catalysts, which was defined by the following equation:

$$E_{ads} = E_{slab,molecule} - E_{slab} - E_{molecule}$$

where, E_{ads} meant the adsorption energy, $E_{slab,molecule}$ meant the energy of slab and molecule after adsorption, E_{slab} meant the energy of the catalyst slab before adsorption and $E_{molecule}$ meant the energy of NH_3 and NO molecule in the gas phase before adsorption.[24,25]

3. Results and discussion

3.1 NH_3-SCR activity of the catalysts

NO conversion over the different catalysts under the simulated flue gas conditions were performed to evaluate the denitration activity of the catalysts. As seen in Fig. 1, the NO conversion of TiO_2–ZrO_2 support was worst and below 50% during the whole reaction temperature range. The catalytic activity of Ce/TiO_2–ZrO_2 catalyst was obviously higher than TiO_2–ZrO_2 support at 300–400 °C, but still unsatisfactory at 150–250 °C. The Cu/TiO_2–
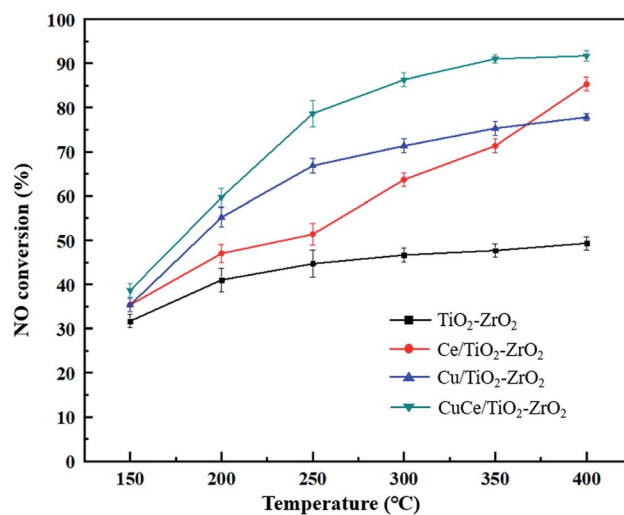

Fig. 1 NO conversion of TiO_2–ZrO_2, Ce/TiO_2–ZrO_2, Cu/TiO_2–ZrO_2 and CuCe/TiO_2–ZrO_2 catalysts.

ZrO_2 catalyst displayed a considerably enhanced activity at low temperature compared with TiO_2–ZrO_2 and Ce/TiO_2–ZrO_2 catalysts. NO conversion on CuCe/TiO_2–ZrO_2 catalyst exceeded 85% at the temperature above 300 °C. Moreover, the low-temperature NH_3-SCR activity of CuCe/TiO_2–ZrO_2 catalyst was markedly higher than other catalysts. It can be observed that copper modification is beneficial to strengthen the low-temperature denitration activity of the cerium-based catalyst. In order to explain the reasons of high NO conversion over CuCe/TiO_2–ZrO_2 catalyst at low temperature interval, XRD, SEM and XPS characterization tests were carried to study textural, morphological and redox properties of the catalysts, and the DRIFTS studies combined with DFT calculations were developed to further explore the adsorption and reaction mechanism of NH_3 and NO on CuCe/TiO_2–ZrO_2 catalyst.

3.2 Textural and morphological analysis

XRD measurement techniques were applied to determine the crystal structure of the catalysts and provide experimental foundation for the catalyst molecular model establishment in subsequent simulation calculation. As the results shown in Fig. 2, TiO_2–ZrO_2 support displays one characteristic peak at $2\theta = 30.5°$, the peak also shown in the XRD patterns of Ce/TiO_2–ZrO_2, Cu/TiO_2–ZrO_2 and CuCe/TiO_2–ZrO_2 catalysts, indicating the presence of $ZrTiO_4$ phase (PDF# 74–1504). The characteristic peaks of (111), (220), (311) crystal faces can be observed in Ce loaded catalysts (PDF# 34-0394), and these diffraction peaks are situated at 28.5°, 47.4° and 56.3°, respectively.[26] For Cu/TiO_2–ZrO_2 and CuCe/TiO_2–ZrO_2 catalysts, there are several diffraction peaks ascribed to CuO crystal structure locate at 32.5°, 35.6°, 38.7°, 48.8°, 53.4°, 58.2°, 61.6°, 66.3°, 68.0°, 72.3°, and 75.2° (PDF# 89-2529).[27] Furthermore, the peak intensity of CuCe/TiO_2–ZrO_2 is weaker than that of Ce/TiO_2–ZrO_2 and Cu/TiO_2–ZrO_2. Thus, it can be concluded that there is strong interaction between CeO_2 and CuO species, and the Cu and Ce active
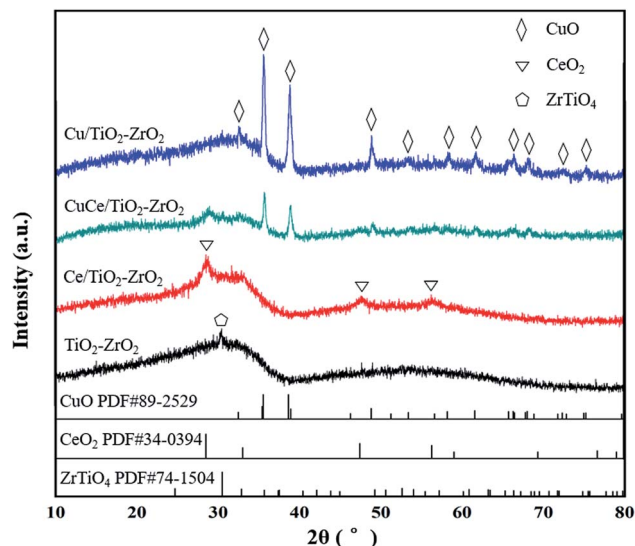
Fig. 2 XRD patterns of TiO₂–ZrO₂, Ce/TiO₂–ZrO₂, Cu/TiO₂–ZrO₂ and CuCe/TiO₂–ZrO₂ catalysts.

components are dispersed well on the CuCe/TiO₂–ZrO₂ catalyst surface.[28]

SEM experiments were conducted to investigate the morphology of the catalysts, and Fig. 3 displays SEM images of various catalysts. It suggests that TiO₂–ZrO₂ presents a block structure loaded with several dense particles. For Ce/TiO₂–ZrO₂ catalyst, CeO₂ particles agglomerate on the part region of the support. However, few particles deposit on the Cu/TiO₂–ZrO₂ catalyst surface. Both above cases will reduce the active surface area of the catalysts. Meanwhile, active components relative uniformly deposit on CuCe/TiO₂–ZrO₂, which is consistent with the XRD results. The high dispersibility is beneficial to increase the active surface area and low temperature denitration activity of the catalyst.

3.3 Redox properties analysis

XPS analysis were performed to investigate the chemical element states of copper and cerium as well as active oxygen species on the raw and modified catalyst surfaces. In the Fig. 4(a), the peaks detected at about 933.8 and 953.6 eV are assigned to Cu $2p_{3/2}$ and Cu $2p_{1/2}$, and some shake-up satellite peaks within 940–945 eV are relevant to Cu^{2+} and polycrystalline Cu_2O species.[29] By the peak deconvolution, the Cu $2p_{3/2}$ splits into two peaks that are located at around 933.6 eV and 935.5 eV while the Cu $2p_{1/2}$ splits into two peaks that are detected at around 953.5 eV and 955.4 eV. The peaks at 933.6 eV and 953.5 eV can be contributed to the Cu^+ species, while the peaks at 935.5 eV and 955.4 eV are corresponded to Cu^{2+} species. The result shows that both Cu^+ and Cu^{2+} coexist in the CuCe/TiO₂–ZrO₂ catalyst, and Cu^+ species may be generated from strong interface between copper oxide with cerium oxide.[30] Fig. 4(b) shows the Ce 3d spectra for the catalysts, and the spectrum can be split into eight components. The peaks denoted as u' and v' are assigned to Ce^{3+}, while the peaks denoted as u, u'', u''', v, v'' and v''' are attributed to Ce^{4+}.[31,32] The existence of Ce^{4+}/Ce^{3+}

redox couple contributes to the better NH₃-SCR activity of the catalyst. Fig. 4(c) illustrates the O 1s spectra of different catalysts. The peak at low binding energy (529.8–530.1 eV) is assigned to the lattice oxygen ($O_β$), and the other peak at high binding energy (531.2–531.6 eV) is regarded as the surface chemisorbed oxygen ($O_α$). It should be mentioned that $O_α$ has been reported to play an important role in low-temperature NH₃-SCR reaction due to its strong mobility.[33]

Table 1 shows the surface chemical composition of the catalysts obtained from XPS spectra. It can be seen that the CuCe/TiO₂–ZrO₂ represents the highest ratio of surface chemisorbed oxygen, which is helpful to improve the low-temperature activity. Besides, the decrease of copper oxidation state and increase of cerium oxidation state coexist on CuCe/TiO₂–ZrO₂ catalyst compared to Ce/TiO₂–ZrO₂ and Cu/TiO₂–ZrO₂ catalysts. Therefore, the synergistic effect of copper and cerium occurs on catalyst surface, which is summarized as follows:

$$Cu^{2+} + Ce^{3+} \leftrightarrow Cu^+ + Ce^{4+}$$
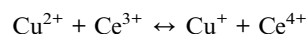
It has been mentioned earlier that surface chemisorbed oxygen contributes to enhance the low-temperature activity, which also accord with the results from Fig. 1 and Table 1. Besides, Ce^{3+} has been confirmed to favor the generation of oxygen vacancies, resulting in a higher proportion of surface chemisorbed oxygen.[34] However, Ce/TiO₂–ZrO₂ catalyst represents a higher ratio of Ce^{3+} and a lower ratio of $O_α$ compared to CuCe/TiO₂–ZrO₂ catalyst. This may be due to the presence of Cu–Ce interface, which promotes the formation of oxygen vacancies and mobility of oxygen species.[35] Therefore, the increased oxygen vacancies caused by the formation of Cu–Ce interface exceed the decreased oxygen vacancies resulted from the reduced Ce^{3+} concentration, causing more surface chemisorbed oxygen generated in CuCe/TiO₂–ZrO₂ catalyst.

The low-temperature activity is also related to the balanced populations of Cu^+/Cu^{2+} sites and dominated by mobile NH₃-solvated Cu species. In the low temperature range, Cu ions can form transient ion pairs and move through NH₃ solvation, thus leading to the better denitration activity. Moreover, the increased ratio of Cu^+/Cu^{2+} leads to the enhanced low-temperature SCR activity.[36] The synergistic effect of copper and cerium also contributes to widen the operating temperature window for the SCR reaction below 300 °C,[30] which leads to the good low-temperature NH₃-SCR activity of the catalyst.

According to the above physicochemical characterization, it is reasonable to conclude that the well dispersed active species and the synergistic effect between Cu and Ce species assist to the improvement in low temperature NH₃-SCR activity of CuCe/TiO₂–ZrO₂ catalyst.

3.4 *In situ* DRIFTS studies

The CuCe/TiO₂–ZrO₂ catalyst with the best catalytic activity was selected for *in situ* DRIFTS characterization to identify the active sites, the adsorbed species and the intermediates on the catalyst surface, aiming at providing the experimental foundation for the adsorption of NH₃ and NO as well as reaction pathways of
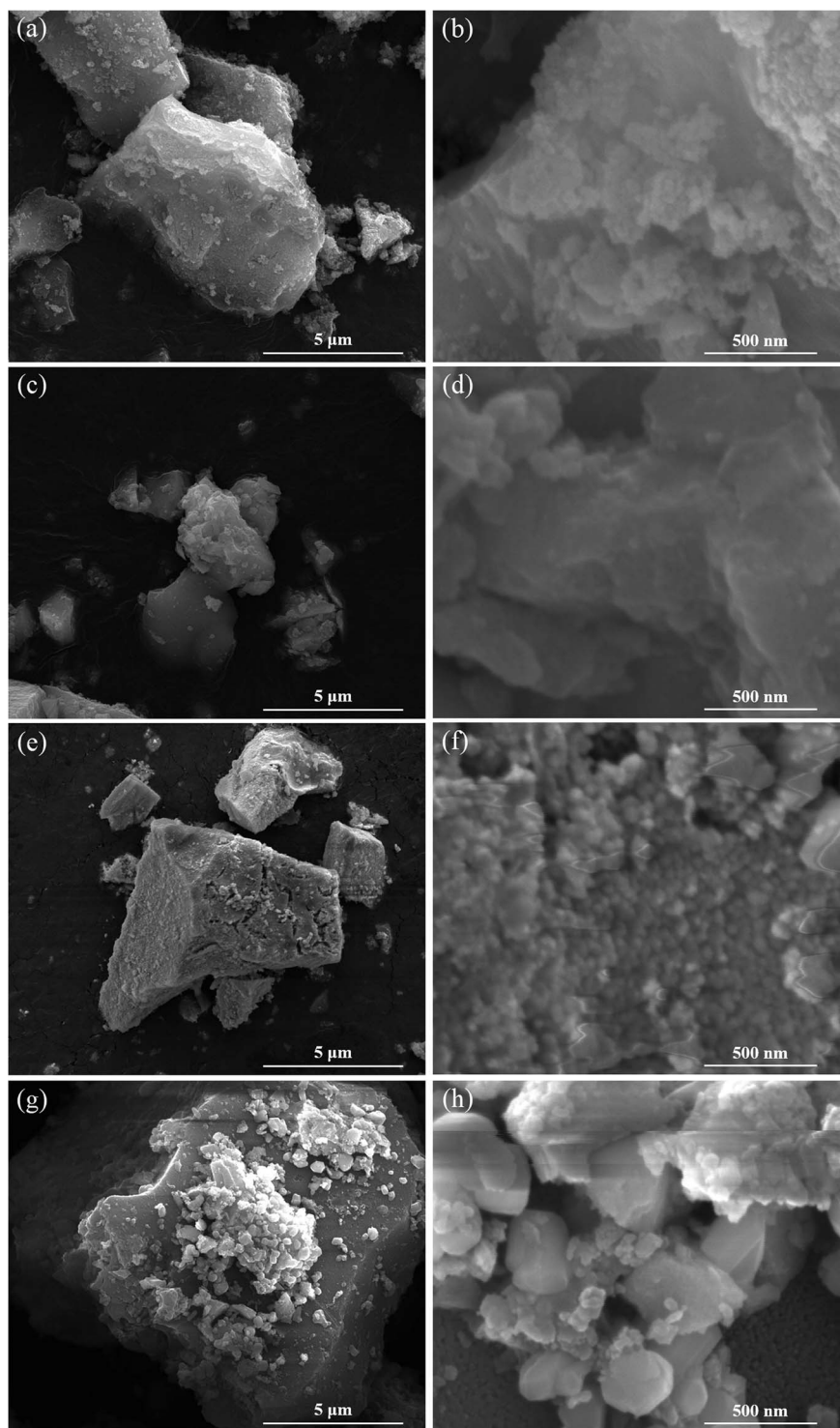
Fig. 3 SEM images of (a and b) $TiO_2–ZrO_2$, (c and d) $Ce/TiO_2–ZrO_2$, (e and f) $Cu/TiO_2–ZrO_2$, (g and h) $CuCe/TiO_2–ZrO_2$ catalyst.

intermediates in DFT calculations, thus figuring out the reaction mechanism of Cu modification on $Ce/TiO_2–ZrO_2$ catalyst in low temperature NH_3-SCR system.

3.4.1 Adsorption of NH_3. *In situ* DRIFTS measurement of the $CuCe/TiO_2–ZrO_2$ catalyst after being exposed to 500 ppm NH_3 for different time at 200 °C was recorded to distinguish the active sites for NH_3 adsorption. Fig. 5 shows the adsorbed NH_3

species over $CuCe/TiO_2–ZrO_2$ surface. When the sample is adsorbed by NH_3 saturation, strong bands at 1606 cm^{-1} and 1207 cm^{-1} can be observed for all the situation, attributed to symmetric and asymmetric N–H bending vibrations of adsorbed NH_3 linked to Lewis acid sites.[37] Besides, the band at 1085 cm^{-1} also represents the symmetric N–H bending vibrations.[38] In the N–H region, several bands are observed at 3372,
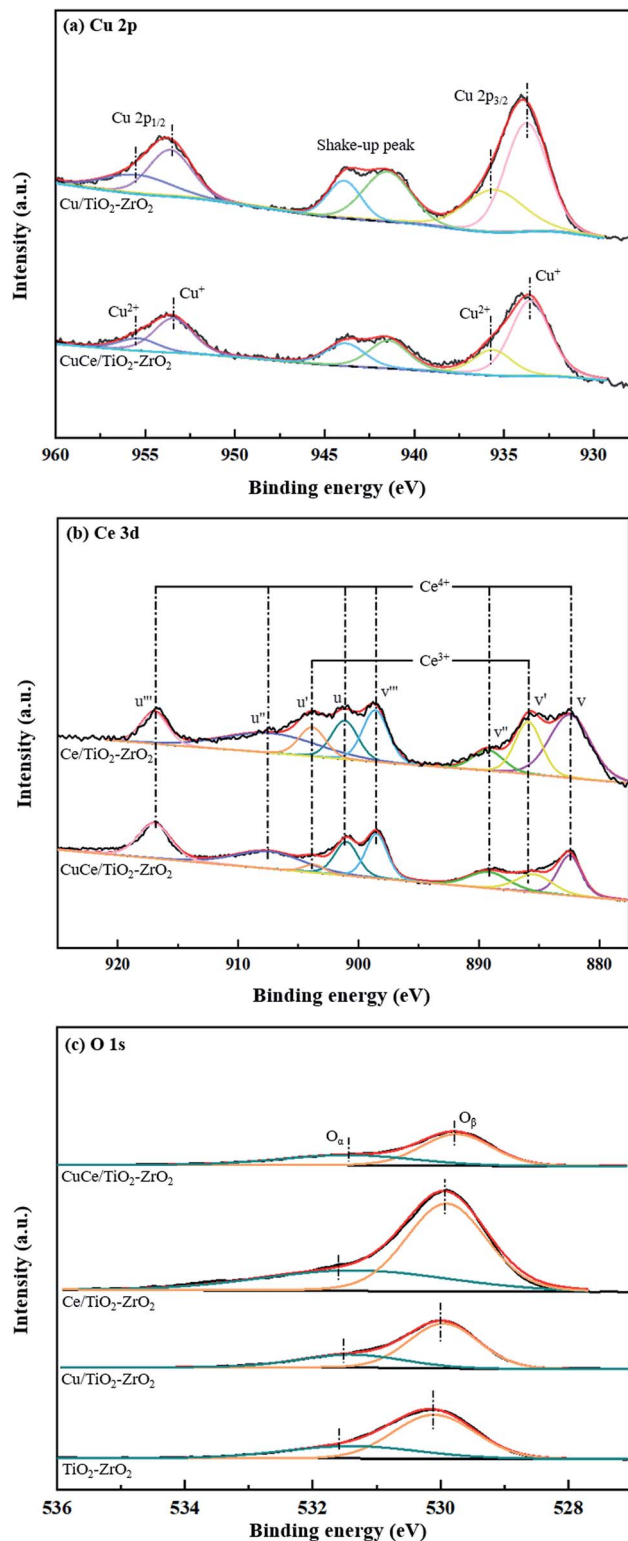
Fig. 4 XPS spectra of the raw and modified catalysts: (a) Cu 2p, (b) Ce 3d, (c) O 1s.

Table 1 Surface chemical composition of the catalysts obtained from XPS spectra

Catalysts	$O_\alpha/(O_\alpha + O_\beta)$	$Cu^+/(Cu^{2+} + Cu^+)$	$Ce^{3+}/(Ce^{3+} + Ce^{4+})$
TiO$_2$–ZrO$_2$	0.314	—	—
Ce/TiO$_2$–ZrO$_2$	0.339	—	0.208
Cu/TiO$_2$–ZrO$_2$	0.301	0.473	—
CuCe/TiO$_2$–ZrO$_2$	0.376	0.554	0.127

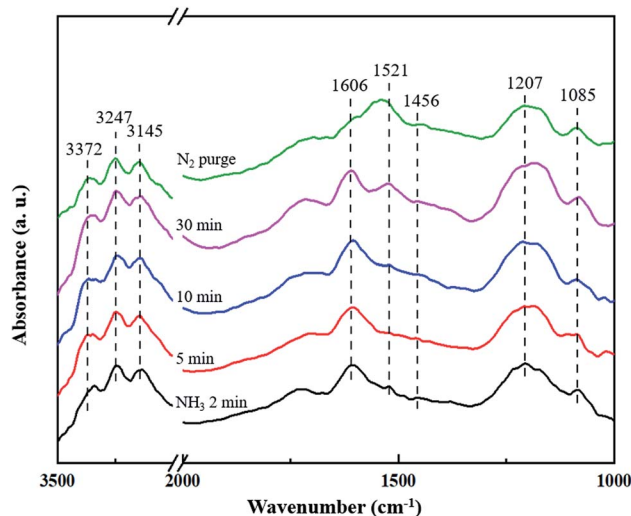Fig. 5 *In situ* DRIFTS spectra of CuCe/TiO$_2$–ZrO$_2$ catalyst treated in flow of 500 ppm NH$_3$ at 200 °C for different times.

band at 1456 cm^{-1} is attributed to the NH$_4^+$ species adsorbed on the Brønsted acid sites,[41] which is much lower than other bands in intensities. All the changes on the states of NH$_3$ adsorption suggest that the quantity of coordinated NH$_3$ on the Lewis acid sites is much larger than that of the NH$_4^+$ ions on the Brønsted acid sites, indicating that NH$_3$ is inclined to adsorb on the Lewis acid sites and NH$_3$ adsorption on the Lewis acid sites is more stable at the reaction process.

3.4.2 Co-adsorption of NO and O$_2$. The co-adsorption of NO and O$_2$ over CuCe/TiO$_2$–ZrO$_2$ catalyst is also investigated by the *in situ* DRIFTS characterization, Fig. 6 displays the spectra obtained with 500 ppm NO + 5% O$_2$ at 200 °C in different time intervals. The bands located at 1170 cm^{-1} and 1029 cm^{-1} are ascribed to the NO$^-$ species and the *cis*-N$_2$O$_2^{2-}$ species, respectively.[42,43] It can be observed that the bands at 1913 cm^{-1} and 1851 cm^{-1} can be detected when catalyst exposed to the NO + O$_2$ atmosphere, and decrease quickly upon the treatment with N$_2$ purge. These bands can be viewed as the gaseous or weakly adsorbed NO linked to the copper sites.[38,44] The bands at 1430 cm^{-1} and 1361 cm^{-1} are both assigned to monodentate nitrate,[42,45] whereas the band at 1567 cm^{-1} is attributed to bidentate nitrate.[46] Moreover, the latter adsorption band is much more intense than the former band, suggesting that the amount of bidentate nitrate is much larger than that of monodentate nitrate. The results show that the bidentate nitrate and
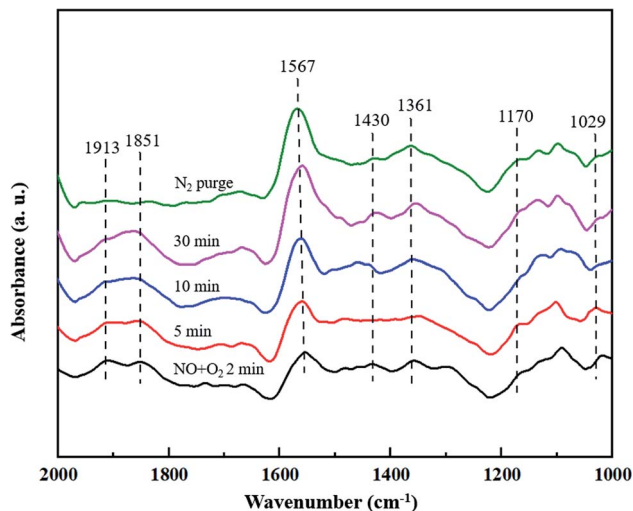
3247 and 3145 cm^{-1}, corresponding to the symmetric and asymmetric N–H stretching vibrations of the coordinated NH$_3$ on Lewis acid sites.[39] Accordingly, the band at 1521 cm^{-1} is assigned to the intermediate of amide species (–NH$_2$).[40] The

Fig. 6 *In situ* DRIFTS spectra of CuCe/TiO$_2$–ZrO$_2$ catalyst treated in flow of 500 ppm NO + 5% O$_2$ at 200 °C for different times.

monodentate nitrate both are the active intermediates on the catalyst surface during NH$_3$-SCR process.

3.5 DFT study

3.5.1 NH$_3$ adsorption on Cu–CeO$_2$ (1 1 1). It has been proved that the NH$_3$ adsorption is the primary factor in the NH$_3$-SCR reaction.[47] NH$_3$ molecules are placed near the Lewis acid sites (Cu–O, Ce1–O, Ce2–O) and Brønsted acid site (Cu–OH) of the catalyst surface to simulate the adsorption process. Surface cerium atoms Ce1 and Ce2 represent Ce-sites of different atomic environment, the former is the Ce atom adjacent to Cu atom and the latter is the Ce atom farther from Cu atom. The optimized geometric structures and energies of NH$_3$ adsorb on the Lewis and Brønsted acid sites are presented in Fig. 7. It can be concluded that the NH$_3$ molecule is more easily combined with the Cu acidic sites (Lewis acid sites). Because the distance between N atom and Cu atom is the shortest (1.922 Å), and the adsorption energy of NH$_3$ adsorbs on the top sites of Cu atom in

the way of the N-down orientation is the lowest (−188.69 kJ mol^{-1}). Compared with Cu sites serve as the Lewis acid sites, NH$_3$ molecule adsorbs on the Brønsted acid site connected with Cu atom has a weaker adsorption capacity, the length of N–H band and O–H band are 2.019 Å and 0.974 Å, and the adsorption energy is −130.70 kJ mol^{-1}. Besides, the bond length of NH$_3$ molecules on the two Ce atoms are 2.693 Å and 2.691 Å, and the adsorption energies of NH$_3$ molecules on the two Ce atoms are −78.56 kJ mol^{-1} and −85.01 kJ mol^{-1}, indicating that the atomic environment has hardly influence on the NH$_3$ adsorption state on the acidic sites. In conclusion, NH$_3$ tends to connect with Lewis acid sites of CuCe/TiO$_2$–ZrO$_2$ catalyst during the reaction process, which is consistent with the *in situ* DRIFT results. Although the Brønsted acid site linked to the Cu atom has higher adsorption energy than that of the Lewis acid site, the adsorption energy is still lower than the adsorption energy of Ce atoms, and the characteristic peak of the NH$_4^+$ ions on the Brønsted acid sites can be detected in NH$_3$ adsorption in *in situ* DRIFTS tests. Therefore, we can speculate that some gaseous ammonia still adsorbs on the Brønsted acid sites.

Taking the above analysis results of NH$_3$ adsorption into consideration, we focus our attention on NH$_3$ dehydrogenation on the Cu atoms in this paper, the potential energy diagram and optimized structures of NH$_3$ dehydrogenation reaction over catalysts are present in Fig. 8, S1,† and Table 2 presents the energy changes of each step involved in the dehydrogenation reaction. On the process, NH$_3$ molecule firstly adsorbs on the top site of Cu atom with its nitrogen end (IM1). H-migration happens after the NH$_3$ adsorption on the catalyst surface, one H atom (H1) of the intermediate Cu–NH$_3$ migrates to the adjacent O atom to form a new Brønsted acid site, the reaction heat is 19.56 kJ mol^{-1} while the activation energy barrier is 49.05 kJ mol^{-1}. Then the NH$_2$ fragment (IM2) continues to lose H atom (H2) to generate NH, the reaction heat is 20.08 kJ mol^{-1} while the activation energy barrier can reach 39.38 kJ mol^{-1}. Finally, NH (IM3) can also be continuously dehydrogenated, one H atom (H3) is transferred to bond with the O atom and only one N atom left on the copper atom (IM4), and the reaction
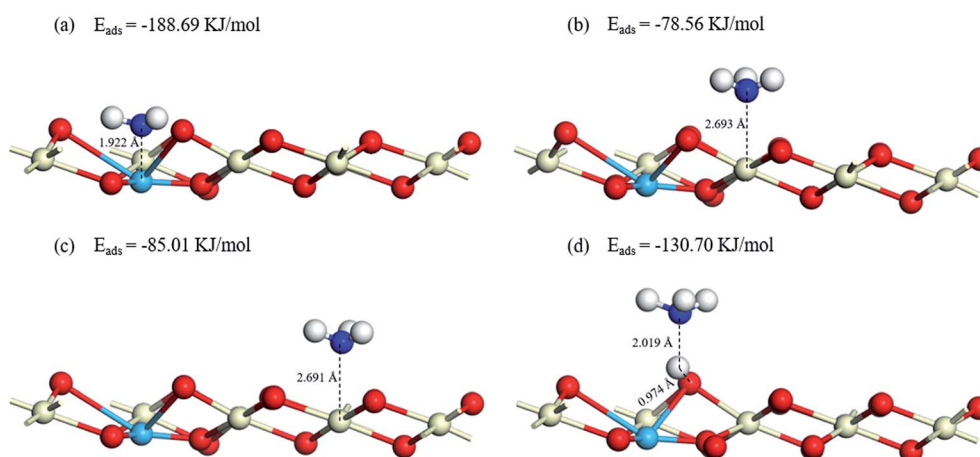

Fig. 7 Optimized structures and energies of NH$_3$ adsorptions on (a) Cu–O, (b) Ce1–O, (c) Ce2–O, (d) Cu–OH.
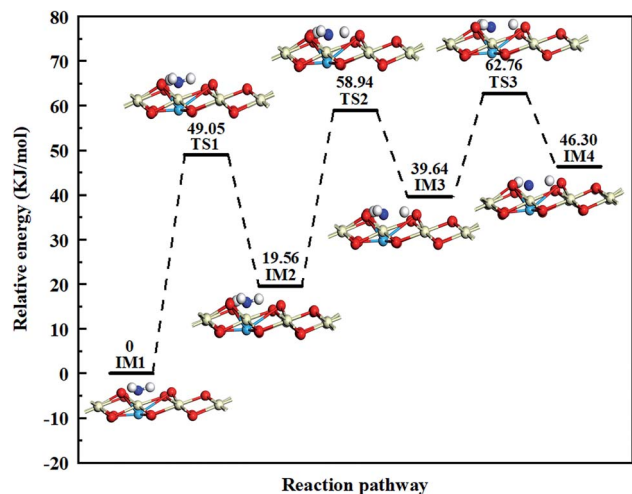
Fig. 8 Potential energy diagram and optimized structures of NH$_3$ dehydrogenation reaction on the Cu atoms. The energy of the reactant is taken as zero.

Table 2 The reaction energies and activation energy barriers of each step involved in the NH$_3$ dehydrogenation reaction on the Cu atoms

	Reaction energy (kJ mol^{-1})	Energy barrier (kJ mol^{-1})
IM1 → TS1 → I M2	19.56	49.05
IM2 → TS2 → IM3	20.08	39.38
IM3 → TS3 → IM4	6.66	23.12

heat is 6.66 kJ mol^{-1} while the activation energy barrier is 23.12 kJ mol^{-1}. The result shows that the activation energy barrier gradually decreases in the NH$_3$ dehydrogenation process, indicating the NH$_3$ dissociation reaction is getting easier. According to the optimized structures of the intermediates and the transition states shown in Fig. S1,† there are symmetric and asymmetric N–H stretching vibrations of the coordinated NH$_3$ on Lewis acid sites during the NH$_3$ dehydrogenation reaction process, which can be verified by the NH$_3$ adsorption results in *in situ* DRIFTS studies. Moreover, the reaction path shows that the NH$_2$ fragment has the lowest energy in the dehydrogenation products, showing it can steadily adsorb on the catalyst surface, which also in harmony with the experimental results.
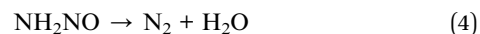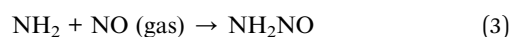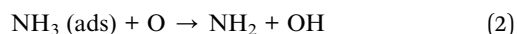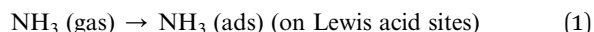
3.5.2 NO adsorption on Cu–CeO$_2$ (1 1 1). Firstly, the adsorption sites of the NO molecule are discussed. Based on the results of NH$_3$ adsorption and dehydrogenation on the catalyst surface, the NH$_2$, NH, N, O1 and O2 active sites are consisted in the adsorption sites (O1 and O2 represent different oxygen active sites at NH$_2$ fragment environment, the former is the O atom in the hydroxyl group and the latter is the O atom adjacent to the Cu atom). The adsorption of the NO molecule is through N-down on, and the optimized adsorption structures and energies of NO molecules adsorb on the catalysts are present in Fig. 9 and S2.† It can be seen that the energies of NO adsorb on NH$_2$, NH, and N are −596.85 kJ mol^{-1}, −609.12 kJ mol^{-1}, and

−610.23 kJ mol^{-1}, respectively. The distances between N atom of NO and Cu atom are 4.145 Å, 2.666 Å, and 3.888 Å for Cu–NH$_2$, Cu–NH, and Cu–N sites. Compared to the NO adsorptions on the N atoms, the NO molecules adsorb on the O atoms have a worse adsorption capacity. The adsorption energies of NO adsorb on O1 and O2 atom are −192.87 kJ mol^{-1} and −333.44 kJ mol^{-1}, but the adsorbed NO molecules have little effect on the adsorbed NH$_3$ molecules on the Lewis acid sites. It suggests that NO molecule is inclined to adsorb on the top sites of N atoms of the dehydrogenation products, and the NH$_2$ and NH$_2$NO intermediates are the important components in the NH$_3$-SCR process.
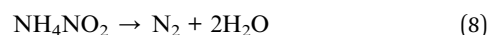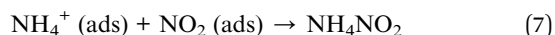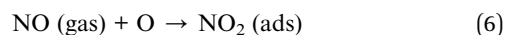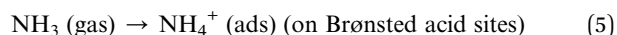
3.6 Proposed reaction mechanism

Combining the experimental and DFT results obtained in this paper and the results of previous studies,[48–53] the NH$_3$-SCR reaction mechanism on CuCe/TiO$_2$–ZrO$_2$ catalyst at low temperature is exhibited and the explanation follows.

The foundational reaction involves the participation of NH$_3$ and NO to generate N$_2$ and H$_2$O, the H atom remained will be connected with the O atom adjacent to Cu atom to form new Brønsted acid site. In detail, the adsorbed NH$_3$ linked to the Lewis acid sites can be activated to form the amino group (–NH$_2$). Then it will further react with gaseous NO to form NH$_2$NO, which is the key intermediate product in the reaction process, and finally decomposes into gas phase N$_2$ and H$_2$O due to instability. The reaction follows Eley–Rideal reaction mechanism and the reaction steps are shown as reaction (1)–(4).

$$NH_3 \text{ (gas)} \rightarrow NH_3 \text{ (ads) (on Lewis acid sites)} \quad (1)$$

$$NH_3 \text{ (ads)} + O \rightarrow NH_2 + OH \quad (2)$$

$$NH_2 + NO \text{ (gas)} \rightarrow NH_2NO \quad (3)$$

$$NH_2NO \rightarrow N_2 + H_2O \quad (4)$$

The regenerative reaction occurs on the Brønsted acid site formed from the foundational reaction, NH$_3$ and NO participate in the reaction to produce N$_2$ and H$_2$O, and the remaining H atom is removed and the Lewis acid site is restored. In this process, gaseous NH$_3$ adsorbs on the Brønsted acid site linked to the Cu atom to form NH$_4^+$ species. At the same time, gaseous NO bonds to the lattice oxygen atom to form monodentate nitrite (–NO$_2$), creating an oxygen vacancy on the catalyst surface, which can be replenished by the active oxygen. Then NH$_4^+$ species migrates to the NO$_2$ to form NH$_4$NO$_2$ intermediate product, and finally decomposes into gaseous N$_2$ and H$_2$O. The reaction follows Langmuir–Hinshelwood reaction mechanism and the reaction steps follow as reaction (5)–(8).
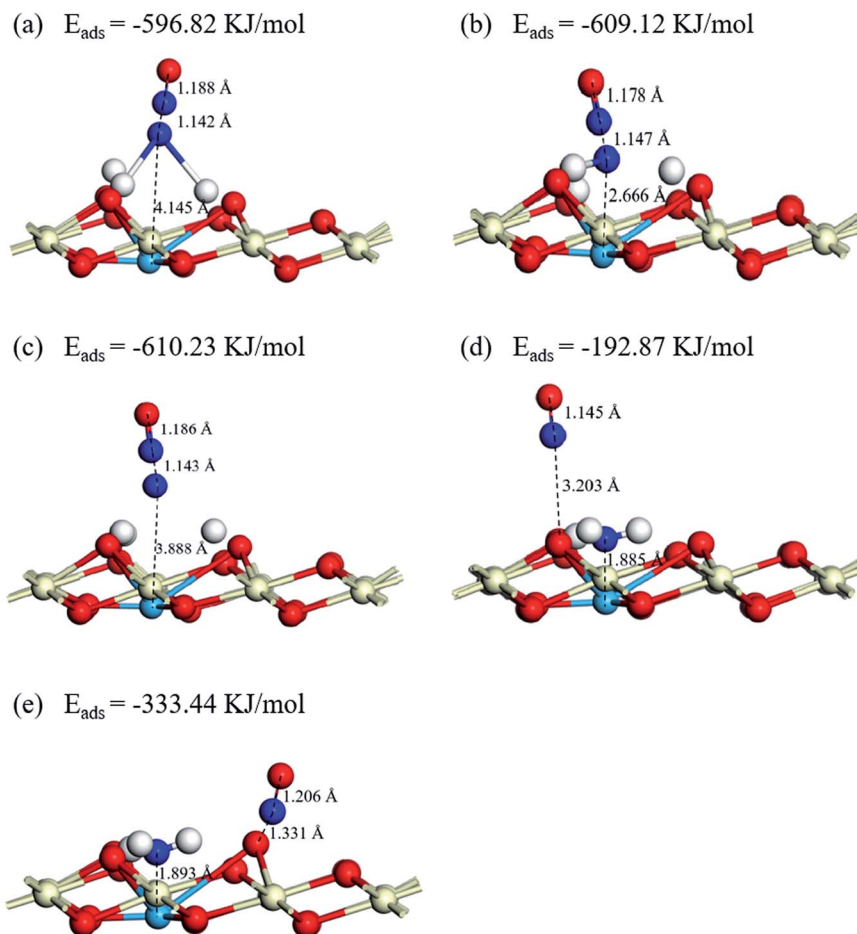
$$NH_3 \text{ (gas)} \rightarrow NH_4^+ \text{ (ads) (on Brønsted acid sites)} \quad (5)$$

$$NO \text{ (gas)} + O \rightarrow NO_2 \text{ (ads)} \quad (6)$$

$$NH_4^+ \text{ (ads)} + NO_2 \text{ (ads)} \rightarrow NH_4NO_2 \quad (7)$$

$$NH_4NO_2 \rightarrow N_2 + 2H_2O \quad (8)$$

(a) E_{ads} = -596.82 KJ/mol

(b) E_{ads} = -609.12 KJ/mol

(c) E_{ads} = -610.23 KJ/mol

(d) E_{ads} = -192.87 KJ/mol

(e) E_{ads} = -333.44 KJ/mol

Fig. 9 Optimized structures and energies of NO adsorptions on (a) Cu–NH$_2$, (b) Cu–NH, (c) Cu–N, (d) NH$_2$–Cu–OH, (e) NH$_2$–Cu–O.

According to the *in situ* DRIFTS and DFT results obtained above, the NH$_3$ adsorption on the Lewis acid sites should be far greater than that on the Brønsted acid sites, suggesting that the Eley–Rideal reaction mechanism dominates in the NH$_3$-SCR reaction process.

As the final summarize comment, the multiple reaction mechanism herein proposed. It is developed from traditional lab-scale experiments and emerging quantum chemical simulations, involving *in situ* DRIFTS of NH$_3$ adsorption and co-adsorption of NO and O$_2$ as well as DFT calculations of NH$_3$ adsorption, NH$_3$ dehydrogenation and NO adsorption on the catalyst surface. The results can be reasonably extended to realistic operating conditions and provide support for the method of experiment combined with simulation in the NH$_3$-SCR mechanism studies. The multiple reaction mechanism (shown in Fig. 10) includes Eley–Rideal reaction mechanism and Langmuir–Hinshelwood reaction mechanism. At low temperatures, the presence of gaseous NH$_3$ ensures the continuous supply to the NH$_3$ adsorption on the catalyst surface. Besides, the NH$_3$ supplement can be divided into two parts to participate in the foundational reaction and regenerative reaction in the NH$_3$-SCR catalytic cycle, and the amount of ammonia involved in the foundational reaction is much higher than that in the regenerative reaction. The NH$_3$ feed will firstly

result in the consumption of the Lewis acid sites, and then, to the activation of the newly generated Brønsted acid sites. Moreover, the Eley–Rideal reaction mechanism dominates in the denitration reaction and the oxidation of NO assists to close the catalytic cycle.
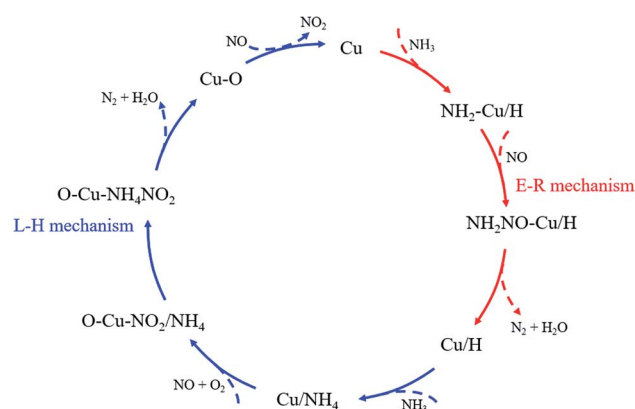

Fig. 10 NH$_3$-SCR catalytic cycle on the CuCe/TiO$_2$–ZrO$_2$ catalyst.

4. Conclusions

In this study, we investigated the improved denitration activity and promotional mechanism of cerium-based catalyst with copper modification in low temperature NH_3-SCR denitration process. $CuCe/TiO_2–ZrO_2$ catalyst has enhanced catalytic activity in the low temperature range comparing to $TiO_2–ZrO_2$, $Ce/TiO_2–ZrO_2$ and $Cu/TiO_2–ZrO_2$ catalysts, which is mainly attributable to the well distributed particulates and synergistic effect of copper and cerium on catalyst surface. The high dispersion degree is helpful to increase the active surface area, and the synergistic effect between copper and cerium (Cu^{2+} + $Ce^{3+} \leftrightarrow Cu^+ + Ce^{4+}$) contributes to increase the ratios of surface chemisorbed oxygen and Cu^+/Cu^{2+}, thus leading to the better low-temperature SCR activity. *In situ* DRIFTS results and DFT calculations were used to study the adsorption and reaction mechanism of NH_3 and NO on the $CuCe/TiO_2–ZrO_2$ catalyst for low-temperature NH_3-SCR reaction. Results show that NH_3 is inclined to adsorb on the Cu acidic sites and the NH_2 and NH_2NO species are the key intermediates in the denitration reaction process. Therefore, copper modification will markedly improve the low temperature denitration activity of cerium-based catalyst. We also reasonably conclude a NH_3-SCR catalytic cycle involving the foundational reaction and regenerative reaction. The Eley–Rideal mechanism and Langmuir–Hinshelwood mechanism both occur in the cycle, and the former mechanism dominates in the denitration reaction.

Author contributions

Wei Zhang: conceptualization, methodology, software, resources, data curation, supervision, project administration, funding acquisition. Yunhao Tang: formal analysis, writing-original draft, writing-review & editing, funding acquisition. Wei Xiao: investigation, visualization, validation. Min Ruan: writing-review & editing, funding acquisition. Yanshan Yin: writing-review & editing, funding acquisition. Quanbin Song: writing-review & editing, funding acquisition. Kang Xie: investigation, visualization. Chuan Qin: investigation, visualization. Mengyao Dong: investigation, validation. Yunhe Zhou: investigation, validation. Jie Li: investigation, validation.

Conflicts of interest

There are no conflicts of interest to declare.

Acknowledgements

References

1 M. Fu, C. Li, P. Lu, L. Qu, M. Zhang, Y. Zhou, M. Yu and Y. Fang, *Catal. Sci. Technol.*, 2014, **4**, 14–25, DOI: 10.1039/C3CY00414G.

2 Y. Yang, Z. Hu, R. Mi, D. Li, X. Yong, H. Yang and K. Liu, *RSC Adv.*, 2019, **9**, 4682–4692, DOI: 10.1039/C8RA10077B.

3 D. Wang, B. Huang, Z. Shi, H. Long, L. Li, Z. Yang and M. Dai, *RSC Adv.*, 2021, **11**, 18458–18467, DOI: 10.1039/d1ra02352g.

4 X. Sun, Q. Liu, S. Liu, X. Zhang and S. Liu, *RSC Adv.*, 2021, **11**, 22780–22788, DOI: 10.1039/d1ra03845a.

5 P. Wang, L. Yao, Y. Pu, L. Yang, X. Jiang and W. Jiang, *RSC Adv.*, 2019, **9**, 36658–36663, DOI: 10.1039/c9ra08640d.

6 S. Xiong, Y. Peng, D. Wang, N. Huang, Q. Zhang, S. Yang, J. Chen and J. Li, *Chem. Eng. J.*, 2020, **387**, 124090, DOI: 10.1016/j.cej.2020.124090.

7 X. Wang, Q. Fang, J. Wang, K. Gui and H. R. Thomas, *RSC Adv.*, 2020, **10**, 44876–44883, DOI: 10.1039/d0ra07351b.

8 H. Zhang, L. Ding, H. Long, J. Li, W. Tan, J. Ji, J. Sun, C. Tang and L. Dong, *J. Rare Earths*, 2020, **38**, 883–890, DOI: 10.1016/j.jre.2020.01.005.

9 P. Nakhostin Panahi, D. Salari, A. Niaei and S. M. Mousavi, *Chin. J. Chem. Eng.*, 2015, **23**, 1647–1654, DOI: 10.1016/j.cjche.2015.08.003.

10 A. Jankowska, A. Chłopek, A. Kowalczyk, M. Rutkowska, W. Mozgawa, M. Michalik, S. Liu and L. Chmielarz, *Microporous Mesoporous Mater.*, 2021, **315**, 110920, DOI: 10.1016/j.micromeso.2021.110920.

11 J. Cheng, S. Han, Q. Ye, S. Cheng, T. Kang and H. Dai, *Microporous Mesoporous Mater.*, 2019, **278**, 423–434, DOI: 10.1016/j.micromeso.2019.01.013.

12 X. Wang, X. Chen, L. Ye, P. Lu, Y. Liu, J. You, W. Zeng, L. Lu, C. Hu and D. Chen, *Mol. Catal.*, 2020, **497**, 111225, DOI: 10.1016/j.mcat.2020.111225.

13 B. Guan, H. Jiang, X. Peng, Y. Wei, Z. Liu, T. Chen, H. Lin and Z. Huang, *Appl. Catal., A*, 2021, **617**, 118110, DOI: 10.1016/j.apcata.2021.118110.

14 L. Li, Y. Wu, X. Hou, B. Chu, B. Nan, Q. Qin, M. Fan, C. Sun, B. Li, L. Dong and L. Dong, *Ind. Eng. Chem. Res.*, 2018, **58**, 849–862, DOI: 10.1021/acs.iecr.8b05066.

15 D. Wang, Y. Peng, S.-c. Xiong, B. Li, L.-n. Gan, C.-m. Lu, J.-j. Chen, Y.-l. Ma and J.-h. Li, *Appl. Catal., B*, 2018, **221**, 556–564, DOI: 10.1016/j.apcatb.2017.09.045.

16 G. Fu, R. Yang, Y. Liang, X. Yi, R. Li, N. Yan, A. Zheng, L. Yu, X. Yang and J. Jiang, *Microporous Mesoporous Mater.*, 2021, **320**, 111060, DOI: 10.1016/j.micromeso.2021.111060.

17 J. Zhou, C. Zhao, J. Lin, H. Yang and R. Zhou, *Catal. Commun.*, 2018, **114**, 60–64, DOI: 10.1016/j.catcom.2018.05.008.

18 Z. Zhao, E. Li, Y. Qin, X. Liu, Y. Zou, H. Wu and T. Zhu, *J. Environ. Sci.*, 2020, **90**, 119–137, DOI: 10.1016/j.jes.2019.11.008.

19 X. Yan, J. Liu, Y. Yang, Z. Wang and Y. Zheng, *Fuel Process. Technol.*, 2021, **216**, 106798, DOI: 10.1016/j.fuproc.2021.106798.

20 S. Chen, M. A. Vasiliades, Q. Yan, G. Yang, X. Du, C. Zhang, Y. Li, T. Zhu, Q. Wang and A. M. Efstathiou, *Appl. Catal., B*, 2020, **277**, 119186, DOI: 10.1016/j.apcatb.2020.119186.

21 Y. Jiang, T. Liu, C. Lai, Z. Yang, R. Lin, X. Wang and X. Zhu, *Appl. Surf. Sci.*, 2021, **547**, 149196, DOI: 10.1016/j.apsusc.2021.149196.

22 J. Wang and X. Gong, *Appl. Surf. Sci.*, 2018, **428**, 377–384, DOI: 10.1016/j.apsusc.2017.09.120.

23 S. Hassan, R. Kumar, A. Tiwari, W. Song, L. v. Haandel, J. K. Pandey, E. Hensen and B. Chowdhury, *Mol. Catal.*, 2018, **451**, 238–246, DOI: 10.1016/j.mcat.2018.01.025.

24 D. Ren, K. Gui and S. Gu, *Appl. Surf. Sci.*, 2021, **561**, 149847, DOI: 10.1016/j.apsusc.2021.149847.

25 D. Ren, K. Gui and S. Gu, *Mol. Catal.*, 2021, **502**, 111373, DOI: 10.1016/j.mcat.2020.111373.

26 Y. Zhou, S. Ren, J. Yang, W. Liu, Z. Su, Z. Chen, M. Wang and L. Chen, *J. Energy Inst.*, 2021, **98**, 199–205, DOI: 10.1016/j.joei.2021.05.006.

27 W. Zhang, Y. Tang, C. Lu, J. Zou, M. Ruan, Y. Yin, M. Qing and Q. Song, *Ultrason. Sonochem.*, 2021, **72**, 105466, DOI: 10.1016/j.ultsonch.2021.105466.

28 R. Guo, W. Zhen, W. Pan, Y. Zhou, J. Hong, H. Xu, Q. Jin, C. Ding and S. Guo, *J. Ind. Eng. Chem.*, 2014, **20**, 1577–1580, DOI: 10.1016/j.jiec.2013.07.051.

29 S. Ali, L. Chen, Z. Li, T. Zhang, R. Li, S. u. H. Bakhtiar, X. Leng, F. Yuan, X. Niu and Y. Zhu, *Appl. Catal., B*, 2018, **236**, 25–35, DOI: 10.1016/j.apcatb.2018.05.014.

30 G. Chi, B. Shen, R. Yu, C. He and X. Zhang, *J. Hazard. Mater.*, 2017, **330**, 83–92, DOI: 10.1016/j.jhazmat.2017.02.013.

31 J. Fan, P. Ning, Z. Song, X. Liu, L. Wang, J. Wang, H. Wang, K. Long and Q. Zhang, *Chem. Eng. J.*, 2018, **334**, 855–863, DOI: 10.1016/j.cej.2017.10.011.

32 Y. Zhang, P. Wu, K. Zhuang, K. Shen, S. Wang and W. Guo, *Materials*, 2019, **12**, 2534, DOI: 10.3390/ma12162534.

33 B. Shen, Y. Wang, F. Wang and T. Liu, *Chem. Eng. J.*, 2014, **236**, 171–180, DOI: 10.1016/j.cej.2013.09.085.

34 C. Santra, A. Auroux and B. Chowdhury, *RSC Adv.*, 2016, **6**, 45330–45342, DOI: 10.1039/C6RA05216A.

35 J. Lu, J. Zhong, Q. Ren, J. Li, L. Song, S. Mo, M. Zhang, P. Chen, M. Fu and D. Ye, *Chin. Chem. Lett.*, 2021, DOI: 10.1016/j.cclet.2021.05.029.

36 N. Zhu, Z. Lian, Y. Zhang, W. Shan and H. He, *Appl. Surf. Sci.*, 2019, **483**, 536–544, DOI: 10.1016/j.apsusc.2019.03.336.

37 L. Chen, Z. Si, X. Wu and D. Weng, *ACS Appl. Mater. Interfaces*, 2014, **6**, 8134–8145, DOI: 10.1021/am5004969.

38 J. Wang, Z. Yan, L. Liu, Y. Chen, Z. Zhang and X. Wang, *Appl. Surf. Sci.*, 2014, **313**, 660–669, DOI: 10.1016/j.apsusc.2014.06.043.

39 K. B. Nam, D. W. Kwon and S. C. Hong, *Appl. Catal., A*, 2017, **542**, 55–62, DOI: 10.1016/j.apcata.2017.05.017.

40 L. Chen, J. Li and M. Ge, *Environ. Sci. Technol.*, 2010, **44**, 9590–959610, DOI: 10.1021/es102692b.

41 S. Xie, L. Li, L. Jin, Y. Wu, H. Liu, Q. Qin, X. Wei, J. Liu, L. Dong and B. Li, *Appl. Surf. Sci.*, 2020, **515**, 146014, DOI: 10.1016/j.apsusc.2020.146014.

42 Q. Zhang, J. Fan, P. Ning, Z. Song, X. Liu, L. Wang, J. Wang, H. Wang and K. Long, *Appl. Surf. Sci.*, 2018, **435**, 1037–1045, DOI: 10.1016/j.apsusc.2017.11.180.

43 Z. Ma, X. Wu, H. Härelind, D. Weng, B. Wang and Z. Si, *J. Mol. Catal. A: Chem.*, 2016, **423**, 172–180, DOI: 10.1016/j.molcata.2016.06.023.

44 K. I. Hadjiivanov, *Catal. Rev.*, 2000, **42**, 71–144, DOI: 10.1081/CR-100100260.

45 S. Liu, P. Yao, Q. Lin, S. Xu, M. Pei, J. Wang, H. Xu and Y. Chen, *Catal. Today*, 2021, **382**, 34–41, DOI: 10.1016/j.cattod.2021.05.007.

46 L. Wei, S. Cui, H. Guo and L. Zhang, *Comput. Mater. Sci.*, 2018, **144**, 216–222, DOI: 10.1016/j.commatsci.2017.12.013.

47 Y. Peng, K. Li and J. Li, *Appl. Catal., B*, 2013, **140–141**, 483–492, DOI: 10.1016/j.apcatb.2013.04.043.

48 L. Wei, S. Cui, H. Guo and X. Ma, *Mol. Catal.*, 2018, **445**, 102–110, DOI: 10.1016/j.mcat.2017.11.022.

49 B. Guan, H. Jiang, Y. Wei, Z. Liu, X. Wu, H. Lin and Z. Huang, *Mol. Catal.*, 2021, **510**, 111704, DOI: 10.1016/j.mcat.2021.111704.

50 H. Wu, M. He, W. Liu, L. Jiang, J. Cao, C. Yang, J. Yang, J. Peng, Y. Liu and Q. Liu, *J. Environ. Chem. Eng.*, 2021, **9**, 105426, DOI: 10.1016/j.jece.2021.105426.

51 S. Wang, R. Guo, W. Pan, Q. Chen, P. Sun, M. Li and S. Liu, *Catal. Commun.*, 2017, **89**, 143–147, DOI: 10.1016/j.catcom.2016.11.005.

52 G. Yang, J. Ran, X. Du, X. Wang, Y. Chen and L. Zhang, *Microporous Mesoporous Mater.*, 2018, **266**, 223–231, DOI: 10.1016/j.micromeso.2018.01.034.

53 F. Gao, C. Yang, X. Tang, H. Yi and C. Wang, *J. Environ. Sci.*, 2022, **113**, 204–218, DOI: 10.1016/j.jes.2021.05.032.